



# Preclinical radiotherapy at the Australian Synchrotron's Imaging and Medical Beamline: instrumentation, dosimetry and a small-animal feasibility study

Jayde Livingstone,<sup>a,\*</sup> Jean-François Adam,<sup>b,c</sup> Jeffrey C. Crosbie,<sup>d,e</sup> Chris J. Hall,<sup>a</sup> Jessica E. Lye,<sup>f</sup> Jonathan McKinlay,<sup>a</sup> Daniele Pelliccia,<sup>d</sup> Frédéric Pouzoulet,<sup>g</sup> Yolanda Prezado,<sup>h</sup> Andrew W. Stevenson<sup>a,i</sup> and Daniel Häusermann<sup>a</sup>

Received 23 December 2016

Accepted 25 April 2017

Edited by A. Momose, Tohoku University, Japan

**Keywords:** radiotherapy; preclinical; dosimetry; imaging.

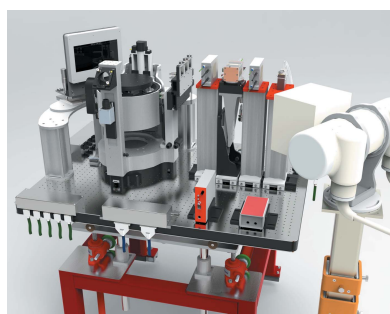
<sup>a</sup>Australian Synchrotron, Clayton, Victoria 3168, Australia, <sup>b</sup>Equipe d'accueil Rayonnement Synchrotron et Recherche Médicale, Université Grenoble-Alpes, Grenoble, France, <sup>c</sup>Centre Hospitalier Universitaire Grenoble-Alpes, Grenoble, France, <sup>d</sup>School of Science, RMIT University, Melbourne, Victoria 3001, Australia, <sup>e</sup>William Buckland Radiotherapy Centre, The Alfred Hospital, Melbourne, Victoria 3004, Australia, <sup>f</sup>Australian Radiation Protection and Nuclear Safety Agency, Yallambie, Victoria 3085, Australia, <sup>g</sup>Département de Recherche Translationnelle, Institut Curie, Orsay, France, <sup>h</sup>Unité Imagerie et Modélisation en Neurobiologie et Cancérologie, Centre National de la Recherche Scientifique, Orsay, France, and <sup>i</sup>CSIRO Manufacturing, Clayton South, Victoria 3168, Australia.

\*Correspondence e-mail: jayde.livingstone@synchrotron.org.au

Therapeutic applications of synchrotron X-rays such as microbeam (MRT) and minibeam (MBRT) radiation therapy promise significant advantages over conventional clinical techniques for some diseases if successfully transferred to clinical practice. Preclinical studies show clear evidence that a number of normal tissues in animal models display a tolerance to much higher doses from MRT compared with conventional radiotherapy. However, a wide spread in the parameters studied makes it difficult to make any conclusions about the associated tumour control or normal tissue complication probabilities. To facilitate more systematic and reproducible preclinical synchrotron radiotherapy studies, a dedicated preclinical station including small-animal irradiation stage was designed and installed at the Imaging and Medical Beamline (IMBL) at the Australian Synchrotron. The stage was characterized in terms of the accuracy and reliability of the vertical scanning speed, as this is the key variable in dose delivery. The measured speed was found to be within 1% of the nominal speed for the range of speeds measured by an interferometer. Furthermore, dose measurements confirm the expected relationship between speed and dose and show that the measured dose is independent of the scan direction. Important dosimetric parameters such as peak dose, valley dose, the collimator output factor and peak-to-valley dose ratio are presented for 5 mm × 5 mm, 10 mm × 10 mm and 20 mm × 20 mm field sizes. Finally, a feasibility study on three glioma-bearing rats was performed. MRT and MBRT doses were prescribed to achieve an average dose of 65 Gy in the target, and magnetic resonance imaging follow-up was performed at various time points after irradiation to follow the tumour volume. Although it is impossible to draw conclusions on the different treatments with such a small number of animals, the feasibility of end-to-end preclinical synchrotron radiotherapy studies using the IMBL preclinical stage is demonstrated.

## 1. Introduction

Therapeutic applications of synchrotron X-rays are becoming a reality. The first clinical trial in synchrotron radiotherapy began in 2012 with phase I/II clinical studies of synchrotron stereotactic radiation therapy at the European Synchrotron Radiation Facility (ESRF). To date, 13 oligo-brain-metastatic patients have been treated using 80 keV high-flux quasi-parallel monochromatic X-ray beams, immediately after



injection of an iodine contrast agent for localized dose enhancement (Balosso *et al.*, 2014). The phase I/II trial is a dose escalation study to demonstrate the feasibility and safety of the technique. Although the technique is still in its infancy, demonstration of the technical feasibility of treating humans at a synchrotron shows promise for the clinical transfer of other synchrotron radiation therapy modalities with improved healthy tissue sparing effects. One realistic option is the use of high-dose-rate arrays of synchrotron microbeams for treating isolated small lesions (Grotzer *et al.*, 2015).

Microbeam radiation therapy (MRT) is an innovative radiotherapy technique that promises significant advantages over conventional methods. It is based on the spatial fractionation of the dose using an array of parallel microbeams. The microbeams typically have a width of several tens of micrometres and are separated by regions of low dose. Preclinical studies have demonstrated that MRT allows significantly increased doses (compared with conventional radiotherapy) to be delivered to the tumour with minimal damage to normal tissues (Bouchet *et al.*, 2013; Ibahim *et al.*, 2016). This is the result of preferential damage to cancerous cells and high tolerance of healthy tissues to the spatially fractionated irradiation pattern. Although MRT is currently confined to synchrotron radiation research due to the very high radiation dose-rate (up to 5000 times higher than clinical radiotherapy) and low divergence required, clinicians and medical researchers are collaborating closely with synchrotron scientists to spearhead its development towards clinical trials.

A similar technique, also based on spatial fractionation of the X-ray beam, known as minibeam radiation therapy (MBRT) has previously been investigated and compared with MRT. As the name suggests, minibeam widths are up to an order of magnitude greater than those typically seen in MRT, which alleviates some of the challenges identified in the transfer of MRT to clinical practice (Dilmanian *et al.*, 2006; Prezado *et al.*, 2012). A tissue-sparing effect, albeit less than that for MRT, has been observed in beams up to 0.68 mm wide (Dilmanian *et al.*, 2006), but the main advantage of MBRT is that it may be more readily transferred to clinics using modified conventional X-ray sources.

The transfer of synchrotron radiotherapy to clinical practice requires rigorous quality assurance based on clinical codes of practice to be implemented on the synchrotron beamlines involved. Such protocols are well established in conventional radiotherapy, but they are not directly applicable to MRT due to radiation detector limitations in submillimetric high-dose-rate kilovolt X-ray fields. Absolute dosimetry protocols traceable to primary standards in medium-energy kilovolt X-rays have recently been proposed and implemented (Lye *et al.*, 2016; Fournier *et al.*, 2016). Additionally, a real-time method for measuring microbeam doses and the peak-to-valley dose ratio using a solid-state detector was developed and benchmarked (Livingstone *et al.*, 2016). In addition to advances in dosimetry, clinical tools such as image guidance (Pelliccia *et al.*, 2016a; Donzelli *et al.*, 2016) and treatment planning systems (Martínez-Rovira *et al.*, 2012; Bartsch & Oelfke, 2013) specific to these innovative radiotherapy

modalities are being developed. These medical physics tools are bringing synchrotron radiotherapy using high-dose-rate spatially fractionated beams closer to clinical practice.

In parallel with these developments, preclinical trials are aiming to answer questions about radiobiological pathways of synchrotron therapy, including tumouricidal mechanisms and normal tissue toxicity. A recent review on the status of normal tissue toxicity data from MRT preclinical trials (Smyth *et al.*, 2016) concluded that very few of the studies previously performed were specifically designed for characterizing the normal tissue response to MRT. Furthermore, despite clear evidence that a number of normal tissues display a tolerance to much higher doses from MRT than conventional radiotherapy, a lack of consistency in the beam geometries, tissue types and doses used in the various studies makes it difficult to quantify the relationship between dose and normal tissue toxicity. A systematic approach to the design and implementation of preclinical trials is essential for the determination of tumour control and normal tissue complication probabilities of MRT.

To address these issues, the Imaging and Medical Beamline (IMBL) at the Australian Synchrotron has designed and installed a dedicated preclinical radiotherapy station on the beamline, for the sole purpose of performing systematic and reproducible dosimetry and *in vivo* studies for synchrotron radiotherapy. In this paper, we describe the preclinical radiotherapy instrumentation, present results from the characterization of this system, report on dosimetry measurements and on a technical feasibility study of MRT and MBRT performed on glioma-bearing rats.

## 2. Materials and methods

### 2.1. Radiotherapy instrumentation

The Imaging and Medical Beamline (IMBL) is one of ten beamlines at the Australian Synchrotron (3 GeV electron energy, 200 mA storage-ring current). The IMBL source is a superconducting multipole wiggler (SCMPW) consisting of 30 pole pairs with 52 mm period and a peak magnetic field of 4.2 T. The standard operating magnetic field of the SCMPW is 3 T (Stevenson *et al.*, 2017). The beamline is 145 m in length and has three experimental hutches. Radiotherapy experiments typically take place in the first two experimental hutches, known locally as hutches 1B and 2B, which are located at 20 m and 32 m from the source, respectively. The focus of this paper is the dedicated preclinical radiotherapy station which resides in hutch 2B at a distance of 32 m from the source.

Radiotherapy is performed using a filtered white beam. IMBL features permanent filtration using chemical vapour deposition (CVD) diamond, graphene and high-density graphite to absorb low-energy photons and avoid an excessive thermal load on beamline components. Additional filters are used to produce a variety of spectra of interest for radiotherapy applications. Full characteristics of the beamline including the available filtration combinations are described

by Stevenson *et al.* (2017). The most commonly used filtration for radiotherapy at IMBL is that referred to as ‘F4’ in Table 3 of the above-mentioned publication, which consists of 2.8 mm of copper in addition to the permanent filtration. This filtration produces a spectrum between 50 and 200 keV, with a peak at 87 keV and a weighted mean energy of 94 keV. The aluminium first half value layer (*i.e.* the thickness of aluminium which will reduce the full or unattenuated intensity of the beam by two) of this spectrum is 13.6 mm. The surface dose-rate (absorbed dose to water) at the sample stage in hutch 2B is approximately  $300 \text{ Gy s}^{-1}$ .

The first radiotherapy-specific component of IMBL is the in-air fast shutter, shown in Fig. 1. The in-air fast shutter has two identical blade units that are operated by pull-up solenoids, which have an activation time of  $\sim 15 \text{ ms}$ . Each unit has an internally water-cooled tungsten blade that is supported and guided by four flat springs. The two units are vertically offset to each other so that in the deactivated state the beam is centred on the first blade but passes over the top of the second blade. In operation, the first blade is fired, allowing the beam to pass through, and the second blade is fired to block the beam at the end of the exposure. The two blades are then deactivated in a sequence that blocks the beam at all times. This method of operation, which is illustrated in Fig. 2, allows uniform exposure vertically across the beam. As the two units are mechanically identical, their responses are very similar and the exposure time is determined only by the delay between firing of the first and second blades. Exposure times down to 1 ms can be reliably achieved. The in-air fast shutter can be translated into and out of the beam and can also be moved

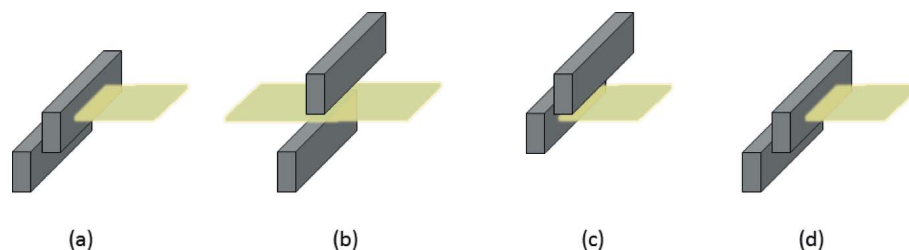


**Figure 2** Schematic diagram illustrating the operation of the in-air fast shutter. In the deactivated state (a), the beam is centred on the first blade but passes over the top of the second blade. To open the shutter, the first blade is activated (b) to allow the beam to pass. At the end of an exposure (c), the second blade is fired to block the beam. Finally, the two blades are deactivated simultaneously (d), blocking the beam at all times.

between different hutches according to the hutch being utilized. It is positioned just upstream of the experimental set-up.

All other radiotherapy components are positioned on a dedicated table within hutch 2B, which is shown in Fig. 3. This table can be translated out of the beam for non-radiotherapy studies and reproducibly replaced in the beam. In this way, it is ensured that the positioning of each component is reliable and reproducible between individual experiments.

The first component on the radiotherapy table is the beam-defining aperture (BDA). The BDA is a slit within a water-cooled tungsten block which ‘cleans up’ X-ray scatter and produces a beam with well defined edges, height and width. BDAs with heights of 0.5, 1 and 2 mm are available and all have a width of 30 mm. As shown in Fig. 3, there are two positions for beam monitors: one immediately upstream of the

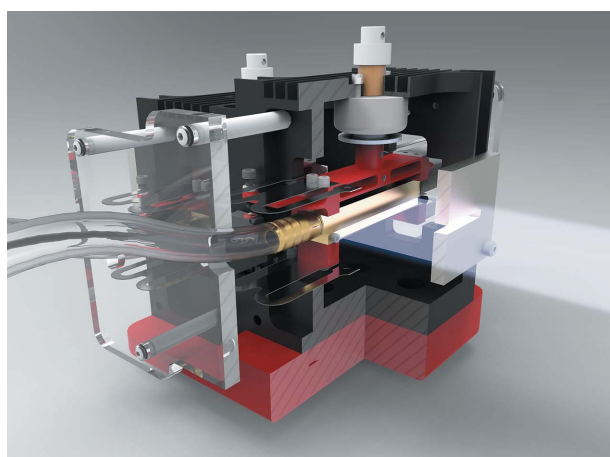


**Figure 1** The IMBL in-air fast shutter for radiotherapy. Two water-cooled tungsten blades move in a way which allows uniform exposure vertically across the beam. Here, the shutter is shown in its deactivated state. The light passing from the right of the image represents the beam.

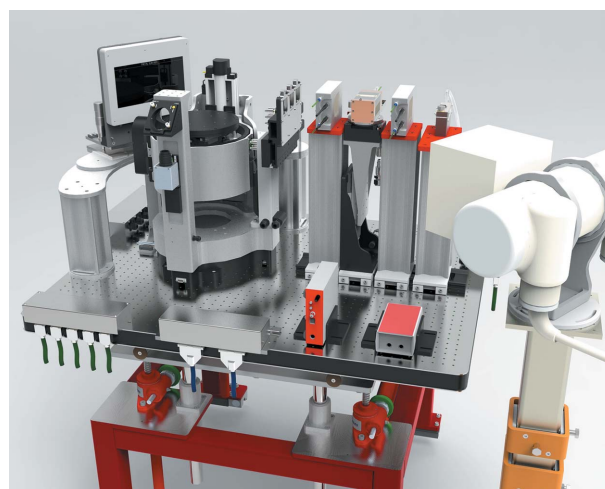


**Figure 3** The IMBL preclinical radiotherapy system. In the front-right of the image is a kilovolt X-ray generator used for image guidance. In the background, from right to left (direction of the beam): beam-defining aperture, upstream beam monitor, collimator for spatially fractionating the beam, downstream beam monitor, small-animal positioning stage incorporating a conformal mask assembly and camera for visually guided positioning, and a flat-panel imaging detector. The beam monitors illustrated here are large-area thin silicon beam monitors.

collimator and the other immediately downstream of the collimator. The purpose of these devices is to monitor the dose rate of the uncollimated and collimated beam. The downstream beam monitor is also used for alignment of the collimator. IMBL has two types of beam monitors that are compatible with this system. The first type is the free air ionization chamber (Advanced Design Consulting USA, Inc.) (Crosbie *et al.*, 2013), whose main advantage is being minimally perturbing to the beam as the only material traversed by the beam is air. The second type is a large-area (5 cm × 5 cm) thin (60 μm) silicon diode (Micron Semiconductor, UK). The diodes have a faster response than the ionization chambers and it is envisaged that they could be used in future in a safety-rated system of interlocks to ensure patient or animal safety.

The collimator used for MRT, the multislit collimator, spatially fractionates the beam into 125 vertical microbeams of 50 μm width with a 400 μm centre-to-centre (c-t-c) spacing. Tungsten carbide layers of 350 μm are sandwiched together to create a 50 μm spacing between them. The multislit collimator is 8 mm thick (in the beam direction), 4 mm high (normal to the beam in the vertical direction) and 40 mm wide (normal to the beam in the horizontal direction). The aluminium housing of the collimator is flushed with helium gas and water-cooled and features kapton entrance and exit windows for negligible beam perturbation. The multislit collimator can be rotated for alignment purposes and can be translated out of the beam when collimation is not required or completely removed to be substituted with a different collimator. Previously, a ‘mini-beam’ collimator has been used for dosimetry (Livingstone *et al.*, 2016) and *in vivo* studies. The minibeam collimator consists of 25 vertical slits with 1200 μm c-t-c spacing cut into a tungsten block which is 10 mm thick, 15 mm high and 40 mm wide. The slits themselves are 600 μm wide separated by 600 μm of tungsten. The minibeam collimator does not require helium flushing or water cooling.

The final component on the radiotherapy table is the small-animal stage. A cutaway diagram illustrating the various components of the stage is given in Fig. 4. The stage has two orthogonal horizontal motors for positioning the target. These motors both have a total range of 50 mm. The horizontal motors are mounted on a rotation axis with a range of 0–270°, so the direction of the horizontal motion relative to the beam depends on the angle. The rotation is used for multiport or ‘crossfired’ irradiations, where the target is irradiated two or more times at different angles relative to the beam. There are also two independent vertical translations. One is used for aligning the target with the centre of the conformal mask, and has a total range of 140 mm. The other, a servo motor, is used for scanning the sample/animal through the beam for the irradiation. As the beam vertical dimensions are much smaller than realistic targets (0.5 to 2 mm compared with 5 to 20 mm), the dose is delivered by scanning the sample vertically through the beam at a constant speed. Since the instantaneous dose rate ( $\dot{D}$ ) is constant in the beam and beam height ( $h$ ) is fixed for a given irradiation, the dose is a function of the scanning velocity ( $v$ ), as shown in equation (1) (Prezado *et al.*, 2011; Lye *et al.*, 2016),

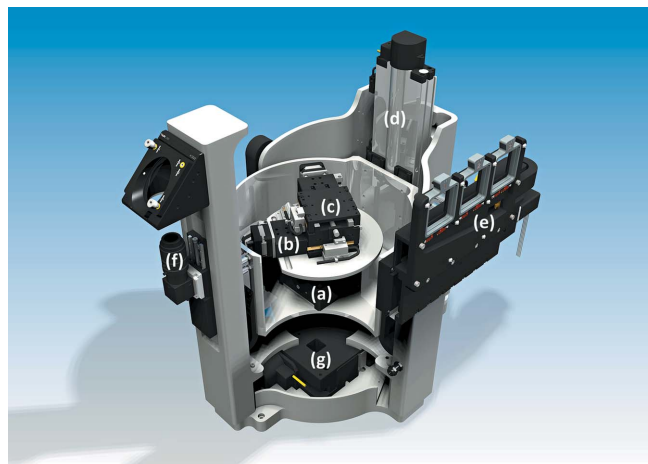


**Figure 4** Cutaway drawing of the small-animal positioning stage for radiotherapy: (a) rotation stage with a range of 0–270°; (b, c) horizontal translation stepper motors mounted perpendicular to each other above the rotation stage with total motion ranges of 50 mm each; (d) vertical translation stepper motor with a range of 140 mm which moves the assembly of (a), (b) and (c) for positioning the target at beam height; (e) mask array with three positions for interchangeable conformal masks which define the irradiation area; (f) colour camera which feeds to the beamline control software for visually positioning the sample or animal; (g) vertical translation servo motor used to scan the entire assembly (stage, mask array and camera) through the beam with a range of 25 mm.

$$D = \dot{D} (h/v). \quad (1)$$

The vertical scanning stage has a total range of 25 mm and maximum speed of 20 mm s<sup>-1</sup>. The reliability of the speed has been measured *via* a Renishaw XL-80 interferometer with a sampling period of 2 ms using the method described by Lye *et al.* (2016).

The conformal mask array has three ports to insert the conformal masks which are used to define the irradiation field. There are a variety of ready-made masks manufactured in 4 mm-thick tungsten available, including square-, circle- and oval-shaped masks with lengths/diameters ranging from 5 mm to 20 mm. User-defined masks of other shapes or sizes can be manufactured from either tungsten or cerrobend (an alloy of bismuth, lead, tin and cadmium). Up to three masks can be inserted into the array at a time and masks can be selected from one of the three ports by translating the array horizontally from the beamline control software. Mechanical switches ensure that the desired port is properly in position. The centre (in the vertical direction) of the mask ports is mechanically fixed and aligned with the beam when the stage is positioned at the centre of its vertical range. When the stage is vertically scanned for an irradiation, the conformal mask(s) move with the stage so that the mask aperture defines the irradiation field impinging on the target.

## 2.2. Sample or animal positioning

Positioned on the side of the stage is a colour camera which feeds to the beamline control software for visually positioning

the target in the beam. The camera is not pointed directly at the target but at a fixed mirror angled at 45° (about the horizontal axis), so that the image on the camera is a reflection of the target. In this way, the camera is protected from scattered radiation. The plane of view of the camera/mirror is perpendicular to the beam axis, so the sample must be rotated by +90° (relative to the beam axis) to obtain a “beam’s eye view” and back to 0° to be in the correct position for irradiation. The image displayed in the beamline control software is interactive and calibrated so that the user can click on the image to position the sample or animal.

A more sophisticated method of sample or animal positioning has been developed by Pelliccia *et al.* (2016a) and uses monochromatic synchrotron X-rays and a Hamamatsu (Hamamatsu Photonics, Hamamatsu City, Japan) flat-panel detector for imaging. This method could in future be extended to take advantage of the enhanced (phase) contrast possible due to the coherence of the X-rays (Pelliccia *et al.*, 2016b). Despite the advantage of enhanced contrast, there are several disadvantages of using the synchrotron beam for image guided positioning. First of all, there is a vertical offset between the white and monochromatic beams, meaning that beamline components must be translated vertically between imaging and treatment procedures. This is not only slow, but introduces a potential for positioning uncertainty as components are moved after positioning. Secondly, the field size is limited by the relatively small width of the beam (30 mm) and range of the stage (25 mm). For these reasons, a kilovolt X-ray tube has been installed next to the beam exit window in hutch 2B. The X-ray tube allows fast larger-area imaging of the animal or sample without any need for vertical translation of beamline components between imaging and treatment procedures.

### 2.3. Dosimetry

Dosimetry is an important requirement for each individual preclinical study. At IMBL, the code of practice for medium-energy kilovoltage X-ray beams proposed by the IAEA TRS-398 (International Atomic Energy Agency, 2000) report has been adopted. IAEA TRS-398 defines ‘medium-energy’ kilovoltage X-ray beams as those with half-value layers greater than 2 mm of aluminium. The code of practice recommends cylindrical ionization chambers as reference dosimeters. A PTW (Freiburg, Germany) Pinpoint 31014 ionization chamber, with a cylindrical cavity of volume 0.015 cm<sup>3</sup>, has been chosen as the IMBL reference dosimeter because it is suitable in fields as small as 20 mm × 20 mm. The chamber has been calibrated in <sup>60</sup>Co beam quality with beam quality correction factors provided for kilovoltage beam qualities with effective energies in the range 35–150 keV. It has also been cross-checked against other ionization chambers and a graphite calorimeter (Lye *et al.*, 2016).

The IAEA TRS-398 report recommends the use of a water phantom for reference dosimetry. A 15.8 cm × 13.7 cm × 12 cm water tank is available at IMBL and is shown in Fig. 5. The tank is made from 6 mm-thick perspex with a 5 cm × 5 cm kapton beam entrance window. The water tank features a

linear motor and a variety of detector holders giving the ability to remotely move the detector along the beam axis for fast and accurate depth dose measurements. Slabs of Gammex (Sun Nuclear Corporation, Melbourne, USA) 457 Solid Water with varying thicknesses are often used, particularly for film dosimetry. Slabs of tissue-mimicking materials such as Gammex 450 cortical bone, Gammex 456 inner bone and Gammex 455 lung are also available. Slabs are available in 10 cm × 10 cm and 20 cm × 20 cm areas and a variety of thicknesses. Dedicated frames are available for the water tank or the solid water phantom which are mounted on the small-animal stage in order to securely hold as well as precisely and reproducibly position the phantoms with their entrance face perpendicular to the beam.

Broad-beam dosimetry is performed using the Pinpoint ionization chamber at 20 mm depth in a solid water or water phantom following the recommendation of the IAEA TRS-398 report. A reference field size of 10 cm × 10 cm is recommended; however, a 20 mm × 20 mm field has been chosen as the reference field size as it is closer to the treatment field sizes for preclinical trials. The Pinpoint chamber is not suitable for dosimetric measurements in fields smaller than 20 mm × 20 mm and does not meet the spatial resolution requirements for resolving microbeam or minibeam peaks. For such measurements, radiochromic film or the PTW micro-Diamond 60019 detector are used. The methods of each have already been described in detail by Livingstone *et al.* (2016).

The active volumes of the detectors are accurately centred on the beam axis using the image guidance procedure described by Pelliccia *et al.* (2016a). For depth dose measurements in the water tank, the linear motor axis is aligned parallel to the beam by acquiring two images of a detector at 5 and 100 mm depths and applying a small angular correction (usually smaller than 1°) calculated from any lateral offset observed between the images. This ensures that the phantom entrance window is parallel to the incoming beam and that the active volume of the detector remains centred

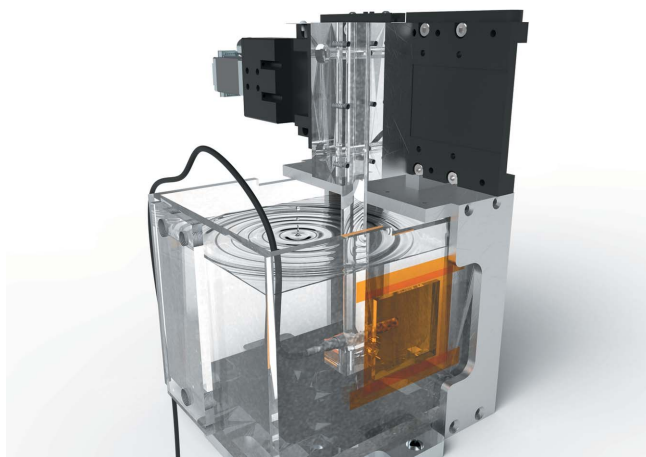


**Figure 5**  
The 15.8 cm × 13.7 cm × 12 cm water tank for dosimetry. The water tank features a linear motor giving the ability to remotely move the detector along the beam axis for depth dose measurements. Holders for a variety of dosimeters are available.

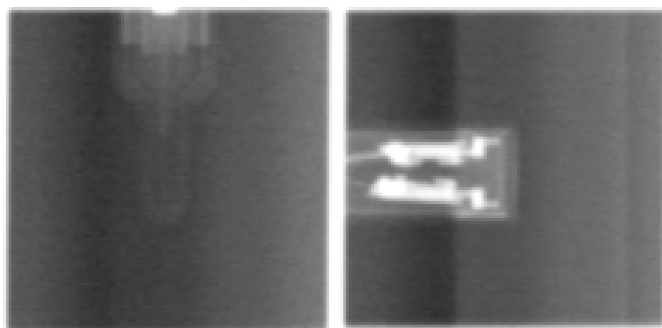


**Figure 6**

Positioning images of the most commonly used dosimetry detectors: Pinpoint (left) and microDiamond (right). The detectors are seen at 5 mm depth in the water tank through a 20 mm × 20 mm field. The active volumes are centred on the beam axis.

on the beam axis at all depths. Example images from this procedure are shown in Fig. 6.

The reproducibility of the dose rate under reference conditions has been studied by performing five identical measurements in separate experiments, using the standard IMBL radiotherapy beam (94 keV mean energy, 3 T wiggler field and 200 mA storage-ring current). The relationship between dose rate and scanning speed was studied by varying the preclinical stage vertical scanning motor speed from 0.1 to 20 mm s<sup>-1</sup> in the downward and upward directions (to investigate the directional dependence) using the PTW Pinpoint detector at 20 mm depth in a water phantom. The upper limit of the speed is dictated by the technical specifications of the motor. The lowest speed of 0.1 mm s<sup>-1</sup> was chosen from dose considerations. The highest dose that can be achieved at this speed, with the smallest beam height (0.5 mm) at the reference depth (20 mm) in water is ~1100 Gy, which is at the maximum end of the range of typical dose prescriptions for preclinical synchrotron radiotherapy studies. It was thus deemed unnecessary to investigate the performance of the stage at lower speeds. For each speed, dose measurements were performed three times. Since from equation (1) the dose has an inverse proportional relationship with velocity, we expect a  $y = C/x$  relationship from a plot of dose against stage velocity, where  $C$  is constant and the product of dose rate ( $\dot{D}$ ) and beam height ( $h$ ).

The microDiamond detector was used to study the dependence of the dose rate on field size (5 × 5, 10 × 10 and 20 mm × 20 mm) and beam height (0.5, 1.0 and 2.0 mm). It was also used to study key dosimetry parameters in spatially fractionated beams, including peak doses, valley doses (the scattered radiation dose delivered between the microbeams), and peak-to-valley dose ratio (PVDR) using the method described by Livingstone *et al.* (2016). A dose profile was acquired by measuring a dose point every 10 μm over a 1.6 mm course centred on the beam axis. The PVDR was calculated from the ratio of the mean dose from four peaks and the mean dose from three valleys, where a valley dose is taken to be the mean dose over the central 100 μm of the valley, as shown in Fig. 7.

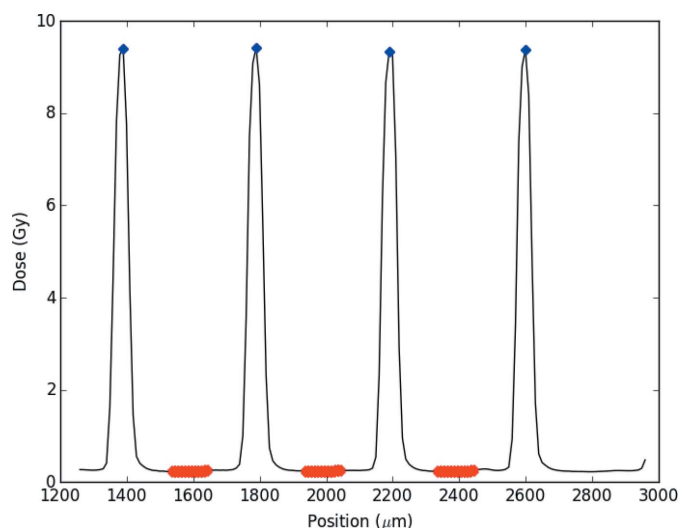


**Figure 7**

Dose profile measured at 20 mm depth in a 10 mm × 10 mm field using the PTW microDiamond detector. One dose point is acquired every 10 μm. The scanning range is 1.6 mm, centred on the beam axis. The PVDR is calculated using the mean of four peak doses and the mean dose in three valleys. The points used for the calculation are represented by the diamond symbols.

The PVDR variation was studied as a function of BDA height for a 20 mm × 20 mm field size with the microbeam collimator in place. The broad-beam doses, microbeam peak doses, valley doses and PVDR values as a function of field size (20 mm × 20 mm, 10 mm × 10 mm and 5 mm × 5 mm) were studied using the 0.5 mm BDA, at various depths in water (5, 10, 20, 30, 40, 50, 100 mm). The collimator output factor, defined as the ratio of microbeam peak dose to broadbeam dose, was also determined for these field sizes and depths.

The versatility of the preclinical stage resides in the possibility of changing the spatial fractionation collimator. This was tested by replacing the MRT collimator by a minibeam collimator (600 μm-wide beams, 1.2 mm c-t-c spacing). Full dose profiles and PVDR values were reported by Livingstone *et al.* (2016) for both microbeam and minibeam collimators for 20 mm × 20 mm and 10 mm × 10 mm field sizes. Doses in the peaks, valleys and the PVDR were found using both collimators for the preclinical study described below.

#### 2.4. Small-animal radiotherapy feasibility study

As a proof of concept of the potential of this experimental preclinical stage, a feasibility experiment was performed on three 7–8 week-old male syngeneic Fischer 344 rats (200–220 g). All operative procedures and animal care were in conformity with the guidelines of the Australian Government and under the approval of the Monash University animal ethics committee agreement (AS-2015-003 – Adam). Each rat was anesthetized by isoflurane inhalation, followed by intraperitoneal infusion of Ketamine Xylazine (60 mg kg<sup>-1</sup> body weight) and xylazine (7 mg kg<sup>-1</sup> body weight). In the present study, the tumours were implanted stereotactically in the right caudate nucleus of the rats [10<sup>4</sup> F98 cells, injected slowly in

5  $\mu\text{L}$  of serum-free Dulbecco's modified eagle medium (DMEM), through a cranial perforation located 3.5 mm to the right of the bregma and at 6 mm depth].

One rat was used as the control animal and remained untreated. For the two other rats, a synchrotron radiotherapy treatment took place on the IMBL preclinical stage, 11 days after tumour implant. One rat was irradiated with crossfired MRT beams (10 mm  $\times$  10 mm field size, 25 microbeams) and the other was irradiated with crossfired MBRT beams (same field size, 8 minibeam). In both cases the dose was prescribed as a 65 Gy integrated dose. For this, a crossfired irradiation of two beams separated by 90° in a 10 mm  $\times$  10 mm field was performed, each delivering 5 Gy or 4.6 Gy at 10 mm depth in the valleys, for MRT and MBRT, respectively, as explained in Fig. 8.

The tumour volume was followed by magnetic resonance imaging (MRI) using T1-weighted images (matrix 256  $\times$  256  $\times$  30, field of view 3 cm  $\times$  3 cm, slice thickness 0.5 mm, echo time 8 ms, repetition time 1600 ms) on the Agilent 9.4 T MRI Small Animal Scanner available at the Monash Biomedical Imaging (MBI) facility after intraperitoneal injection of 0.1 ml of Dotarem gadolinium contrast agent (0.5 mMol ml<sup>-1</sup>; Gerbet, France). The images were acquired on days 9, 14, 17, 23 and 27 days after tumour implantation. The rats were then euthanized after the last MRI by an overdose of anesthetics, since this feasibility study involved only a four-week follow-up of the three animals. The Monash Biomedical Imaging MRI scanner is located in the building immediately next to the IMBL animal facility which makes the imaging follow-up convenient and without stress for the animals.

The aim of the feasibility study was to perform an end-to-end investigation with a small group of live animals using the preclinical stage. This small study is a precursor to a full

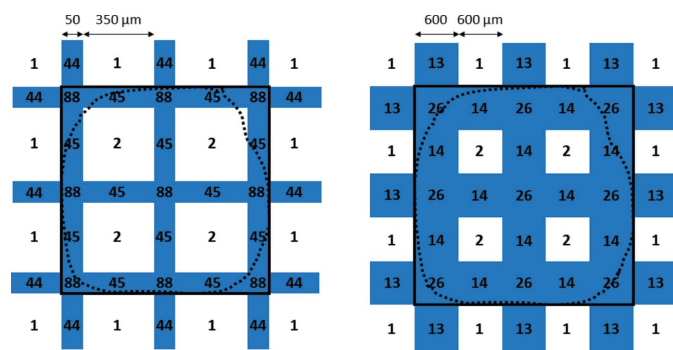


**Figure 8** Crossfired irradiation geometries as seen in the axial plane for MRT (left) and MBRT (right). The target outline is represented by the dotted line and the crossfired area is represented by the thick solid line. The numbers represent a dose (in Gy) for each region, based on a simplified case with a hypothetical valley dose of 1 Gy for each modality, so that the values in the peaks are equivalent to the corresponding PVDRs for the treatment depth and field size. The integrated doses for these simplified cases are 12.75 Gy and 14 Gy for MRT and MBRT, respectively. The beam attenuation has been neglected over the target dimensions for simplification purposes. In the feasibility study, an integrated dose of 65 Gy was prescribed to 10 mm depth in water using a 10 mm  $\times$  10 mm field size. This corresponds to real valley doses of 5 Gy and 4.6 Gy for MRT and MBRT, respectively.

**Table 1** Accuracy of the sample vertical scanning speed measured by interferometry with a 2 ms sampling period in downwards scanning mode. The uncertainties represent two standard deviations.

Nominal velocity (mm s <sup>-1</sup> )	Average velocity (mm s <sup>-1</sup> )	Maximum deviation from mean velocity (%)
20	19.9666 $\pm$ 0.0028	1.3
10	9.9835 $\pm$ 0.0008	2.3
3	2.9950 $\pm$ 0.0002	7.8
1	0.9982 $\pm$ 0.0002	19.7
0.3	0.2992 $\pm$ 0.0002	67.8
0.1	0.0997 $\pm$ 0.0000	162.3
0.01	0.0099 $\pm$ 0.0000	219.3

investigation using a larger group of animals to test the hypothesis that, for the same average dose, crossfired MRT will provide improved tumour control and normal tissue sparing compared with crossfired MBRT. The number of animals involved in this feasibility is not large enough to conclude on any biological outcomes of the spatially fractionated treatments but only on the feasibility of performing end-to-end reproducible radiobiology preclinical trials for synchrotron radiotherapy.

### 3. Results

#### 3.1. Accuracy and reliability testing of animal stage velocity

For a constant dose-rate and beam height, the dose delivered to the animal or sample is a function of just one variable: the speed at which the stage is scanned. In order to deliver the dose accurately and reliably it is thus important to be sure that the velocity is accurate and reliable and that the measured dose varies with speed according to equation (1). It is also important to know the range of speeds for which we are confident that the dose is accurately delivered.

Although the animal stage is fitted with encoders to accurately determine the position, from which the velocity could be determined, the speed of the stage was measured independently *via* interferometry. The results are given in Table 1.

The average speed measured using the interferometer deviates from the nominal speed by less than 1% for speeds between 0.01 and 20 mm s<sup>-1</sup>. Despite the low standard deviation values, large deviations in the instantaneous speed were observed. These ranged from 1–2% of the mean value for speeds of 10–20 mm s<sup>-1</sup>, up to 200% of the mean value for 0.01 mm s<sup>-1</sup>. The amplitude of the deviation was highly dependent on the sampling rate and, as the interferometer is sensitive to vibrations, these uncertainties probably include internal vibration components as well as true instantaneous speed variations. These results suggest that the accuracy of the sample stage speed should also be verified with dose measurements.

#### 3.2. Dosimetry

The dose rate under reference conditions, as measured with the Pinpoint chamber in water at 20 mm depth in a 20 mm  $\times$

**Table 2**

Investigation of the relationship between stage velocity, including directional dependence, and dose (field size 20 mm × 20 mm, beam height 0.5 mm) measured using the Pinpoint detector.

Stage speed (mm s <sup>-1</sup> )	Measured dose (Gy), down direction	Measured dose (Gy), up direction
20	5.63 ± 0.17	5.63 ± 0.17
15	7.51 ± 0.23	–
10	11.28 ± 0.34	11.27 ± 0.34
5	22.54 ± 0.68	22.54 ± 0.68
2	56.39 ± 1.70	–
1	112.70 ± 3.40	112.67 ± 3.39
0.5	225.18 ± 6.78	225.23 ± 6.79
0.1	1124.11 ± 33.86	–

20 mm broad-beam for five different experiments performed over one year is equal to 238 ± 3 Gy s<sup>-1</sup> (one standard deviation). This value is in agreement with the value of 244 ± 9 Gy s<sup>-1</sup> reported by Lye *et al.* (2016) from graphite calorimetry. These measurements have been performed periodically to test and ensure the reproducibility of the system between experiments.

The reproducibility of the measurements within one single experiment was tested twice, with a one-year delay between the two measurements, to ensure the stability of the system. In these measurements, a series of ten dose measurements were taken with the Pinpoint detector in a water phantom under reference conditions. For the two experiments, a combined standard uncertainty of 3.0% (coverage factor  $k = 2$ ) was found. The primary contributors to this uncertainty are the uncertainties quoted for the  $N_{D,w}$  and  $k_Q$  factors of the Pinpoint detector, which are each quoted by the calibration laboratory to be 2.1% ( $k = 2$ ). This result indicates that the dose is accurately delivered and that the system has demonstrated stability over this period of time.

To complement the interferometric velocity measurements, dosimetric measurements were performed with the Pinpoint detector for sample stage vertical scanning speeds between 0.1 and 20 mm s<sup>-1</sup> in the upward and downward scanning directions. The results are shown in Table 2.

From these results we observe that the same dose is measured for a given speed irrespective of the direction it is scanned. The uncertainty in the dose measurements also remains approximately constant for the various speeds, ~3%. A rational function of the form

$$\text{Dose} = 112.4 [\text{Gy s}^{-1} \text{ mm}] / \text{Velocity}$$

was fitted with  $R^2 = 1$ . The large deviations observed in the instantaneous speed observed in Table 1 do not affect the average dose measured with the Pinpoint.

The dose rate as a function of beam height is shown in Table 3 for three different square field sizes (20 mm × 20 mm, 10 mm × 10 mm and 5 mm × 5 mm). They have been measured with the microDiamond detector at 20 mm depth in water. The dose rate measured with the microDiamond for a 20 mm × 20 mm field agree with the above-mentioned Pinpoint dose-rate measurements within 3%. This justifies the use of the microDiamond for accurate absolute dose

**Table 3**

Investigation of the relationship between dose rate and beam height for three different square field sizes (20 mm × 20 mm, 10 mm × 10 mm and 5 mm × 5 mm) measured with the microDiamond detector.

Beam height (mm)	$\dot{D}$ (Gy s <sup>-1</sup> ), 20 mm × 20 mm	$\dot{D}$ (Gy s <sup>-1</sup> ), 10 mm × 10 mm	$\dot{D}$ (Gy s <sup>-1</sup> ), 5 mm × 5 mm
0.5	235.43 ± 11.70	210.00 ± 10.90	194.06 ± 9.65
1.0	244.28 ± 12.14	218.94 ± 10.90	201.42 ± 10.01
2.0	235.01 ± 11.68	210.07 ± 10.44	194.19 ± 9.65

measurements in small fields. There were no significant differences in the dose rates between the various BDAs when considering the associated uncertainties. However, the 1 mm beam height consistently produced a 3.7% higher dose rate when compared with 0.5 or 2 mm beams. The field size output factors are 0.895 and 0.825 for the 10 mm × 10 mm and 5 mm × 5 mm field, when compared with the reference 20 mm × 20 mm field, and are independent of the beam height.

Broad-beam, peak and valley doses, PVDR and collimator output factors (the ratio of microbeam peak dose to broad-beam dose) for various depths in water are shown in Table 4 for a 5 mm × 5 mm field, in Table 5 for a 10 mm × 10 mm field and in Table 6 for a 20 mm × 20 mm field. Field size output factors can be inferred from the results. The results are shown for the 0.5 mm beam height only since the PVDR and output factors values were found constant with beam height. We retrieve classical depth dose information for the broad-beam, peak and valley doses. The valley depth dose exhibits a small ‘build-up’ region where the photon scatter equilibrium is reached after approximately 10 mm of water. The PVDR decreases significantly with increasing field size and depth in water as expected due to the increase in scattered radiation.

### 3.3. Small-animal radiotherapy feasibility study

Dosimetric parameters specific to the conditions for the feasibility study treatment were also measured with the microDiamond detector in the water phantom. Dose profiles were acquired at 10 mm depth in water (the radiological depth of the tumour) in the 10 mm × 10 mm treatment field for MRT and MBRT and are shown in Figs. 9 and 10, respectively.

The PVDRs for a 10 mm × 10 mm field at 10 mm depth were 43.9 ± 0.8 and 12.9 ± 0.1 for the microbeams and minibeam, respectively. This means that at the target depth, for an integrated dose of 65 Gy, the valley doses are 5.07 and 4.65 Gy for MRT and MBRT, respectively, and the peak doses are 222 and 60 Gy, respectively.

X-ray images from the completion of the image-guidance procedure (*i.e.* with the target centred in the treatment field) are shown in Fig. 11. In these images we can clearly see that the rat is well positioned as the field stops in the midline and is centred on the bregma. The upper field limits are set at the surface of the bone at the bregma level. The fields are thus accurately positioned in order to irradiate the right hemisphere with two crossfired MRT or MBRT beams.

The MRI follow-up of the three rats (control, MRT, MBRT) before and after irradiation is shown in Fig. 12. These T1

**Table 4**

Broad-beam, peak and valley doses as a function of depth for 5 mm × 5 mm field size, 0.5 mm beam height and 10 mm s<sup>-1</sup> scan speed measured with the microDiamond detector.

Depth (mm)	Broad-beam dose (Gy)	Peak dose (Gy)	Valley dose (Gy)	Collimator output factor	PVDR
5	14.10 ± 0.63	12.59 ± 0.57	0.168 ± 0.008	0.89 ± 0.06	73.30 ± 1.68
10	12.96 ± 0.58	11.59 ± 0.52	0.168 ± 0.008	0.89 ± 0.06	67.96 ± 1.55
20	11.04 ± 0.50	9.73 ± 0.44	0.147 ± 0.007	0.88 ± 0.06	64.44 ± 1.67
30	9.32 ± 0.42	8.02 ± 0.37	0.137 ± 0.006	0.88 ± 0.06	60.33 ± 1.67
50	6.59 ± 0.30	5.77 ± 0.26	0.100 ± 0.005	0.88 ± 0.06	57.86 ± 1.14
100	2.77 ± 0.12	2.46 ± 0.11	0.043 ± 0.002	0.89 ± 0.06	57.08 ± 1.05

**Table 5**

Broad-beam, peak and valley doses as a function of depth for 10 mm × 10 mm field size, 0.5 mm beam height and 10 mm s<sup>-1</sup> scan speed measured with the microDiamond detector.

Depth (mm)	Broad-beam dose (Gy)	Peak dose (Gy)	Valley dose (Gy)	Collimator output factor	PVDR
5	14.77 ± 0.66	12.65 ± 0.57	0.252 ± 0.011	0.86 ± 0.06	49.81 ± 0.80
10	13.85 ± 0.62	11.69 ± 0.53	0.263 ± 0.012	0.84 ± 0.06	43.90 ± 0.69
20	11.81 ± 0.53	9.85 ± 0.44	0.252 ± 0.011	0.83 ± 0.06	39.76 ± 0.64
30	10.06 ± 0.45	8.26 ± 0.37	0.221 ± 0.010	0.82 ± 0.06	37.84 ± 0.68
50	7.17 ± 0.32	5.85 ± 0.26	0.168 ± 0.007	0.82 ± 0.06	35.87 ± 0.47
100	3.07 ± 0.14	2.48 ± 0.11	0.074 ± 0.003	0.81 ± 0.06	34.25 ± 0.42

**Table 6**

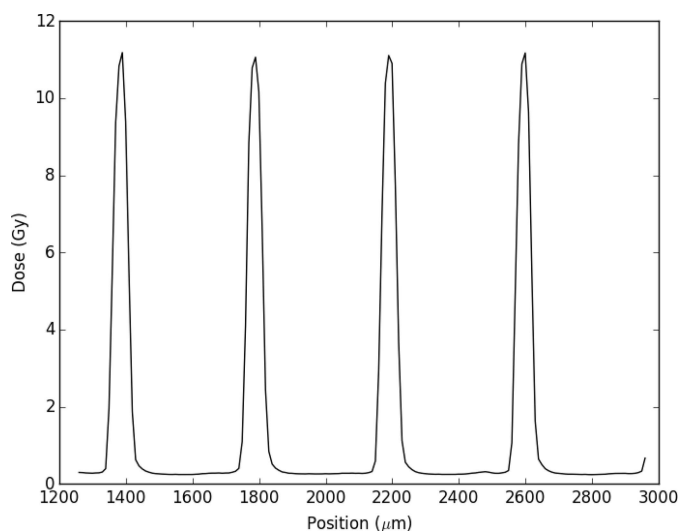
Broad-beam, peak and valley doses as a function of depth for 20 mm × 20 mm field size, 0.5 mm beam height and 10 mm s<sup>-1</sup> scan speed measured with the microDiamond detector.

Depth (mm)	Broadbeam dose (Gy)	Peak dose (Gy)	Valley dose (Gy)	Collimator output factor	PVDR
5	15.71 ± 0.71	12.83 ± 0.58	0.347 ± 0.016	0.82 ± 0.06	36.52 ± 0.46
10	15.00 ± 0.68	11.75 ± 0.53	0.389 ± 0.018	0.78 ± 0.06	30.51 ± 0.36
20	13.18 ± 0.59	9.95 ± 0.45	0.389 ± 0.018	0.76 ± 0.05	25.79 ± 0.30
30	11.34 ± 0.51	8.38 ± 0.38	0.357 ± 0.016	0.74 ± 0.05	23.56 ± 0.29
50	8.25 ± 0.37	5.97 ± 0.27	0.273 ± 0.012	0.72 ± 0.05	21.72 ± 0.33
100	3.59 ± 0.16	2.55 ± 0.11	0.137 ± 0.006	0.71 ± 0.05	18.86 ± 0.17

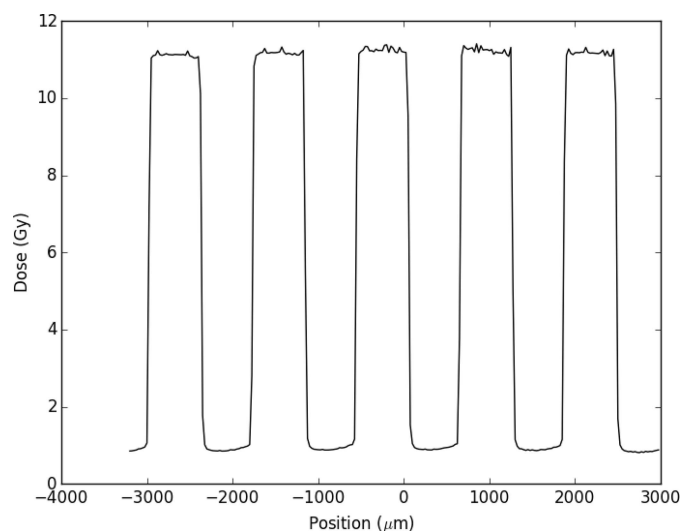
images are axial slices acquired at the isocentre level. These images are used to calculate the tumour volume as a function of time. The associated tumour volumes given as a function of time after implantation are shown in Table 7. Despite having a smaller tumour volume at the beginning of the follow-up, the tumour volume for the control rat was observed to grow exponentially, whereas for the MRT- and MBRT-treated rats the tumour volume stabilized for a week after the treatment and started growing again but at a slower rate. It is obviously impossible to draw conclusions from this feasibility study, because only one rat was irradiated per group and the doses should be optimized for improved tumour control. Further studies are required with large groups of animals in order to reach any definite conclusions or statistical significance regarding the efficacy of MRT and MBRT. However, these results clearly show the feasibility of end-to-end preclinical studies using the IMBL preclinical stage and the follow-up imaging modalities available at the Monash Biomedical Imaging facility.

#### 4. Discussion

There is undoubtedly an interest in the use of high-dose-rate synchrotron



**Figure 9**  
Microbeam dose profile measured at 10 mm depth in water in a 10 mm × 10 mm field size to calculate the PVDR for the treatment conditions. The PVDR is 43.9.

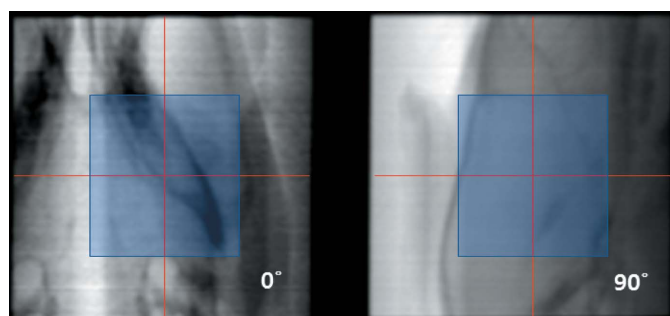


**Figure 10**  
Minibeam dose profile measured at 10 mm depth in water in a 10 mm × 10 mm field size to calculate the PVDR for the treatment conditions. The PVDR is 12.9.

**Table 7**

Tumour volume ( $\text{mm}^3$ ) as a function of time (days) after tumour implantation for each of the study groups.

Irradiation modality	Day 9	Day 14	Day 17	Day 23	Day 27
Control	6	48	135	437	–
MRT	16	55	58	181	306
MBRT	16	52	63	161	314

**Figure 11**

These images at 0 and 90° (*i.e.* parallel and perpendicular to the beam axis) illustrate that the target is well centred in the treatment field following the image guidance procedure.

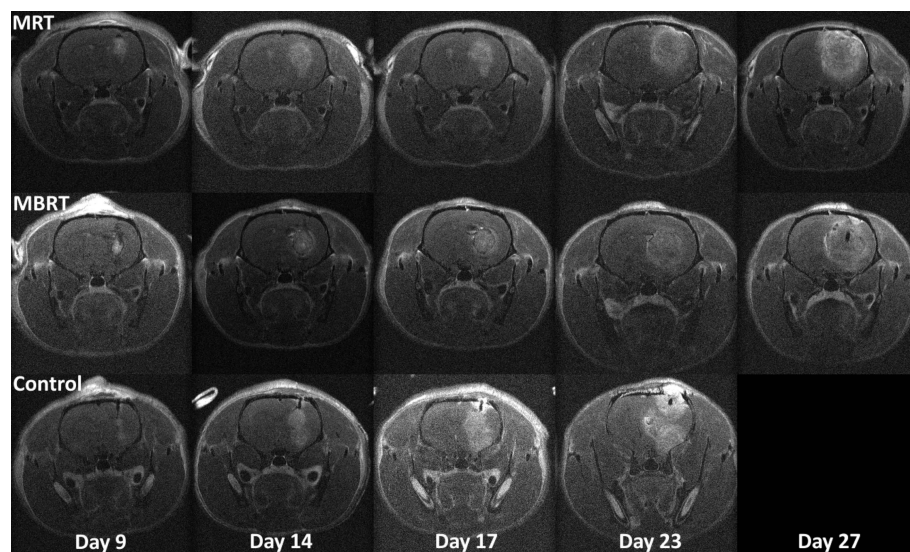
X-rays for radiotherapy applications. The high dose-rate is of particular interest for studying the so-called flash phenomenon (Favaudon *et al.*, 2014) or radiotherapy using spatially fractionated beams such as MRT (Serduc *et al.*, 2010) or MBRT (Deman *et al.*, 2012). In particular, MRT provides encouraging results in oncology (Bouchet *et al.*, 2016) and in epilepsy (Pouyatos *et al.*, 2016) studies. The recent advances addressing medical physics issues related to MRT, in particular in treatment planning (Martínez-Rovira *et al.*, 2012; Bartsch & Oelfke, 2013), experimental dosimetry (Lye *et al.*, 2016;

Fournier *et al.*, 2016; Livingstone *et al.*, 2016) and image guidance (Pelliccia *et al.*, 2016a; Donzelli *et al.*, 2016), make the transfer of this technique to clinical trials realistic within the next decade. However, there is a serious lack of consistency in the preclinical trials associated with MRT, which for now do not allow us to quantify the dose limits that can be reached with this technique in normal tissues or how to prescribe and report the dose. A recent review summarizing 20 years of *in vivo* studies performed in MRT (Smyth *et al.*, 2016) emphasizes this. The lack of consistency in the literature is due, at least partly, to the lack of a dedicated preclinical synchrotron radiotherapy facility, making it difficult to achieve reproducible results.

A dedicated preclinical stage for synchrotron radiotherapy was installed on the Imaging and Medical Beamline. In this paper we have demonstrated the reproducibility, repeatability and accuracy of irradiation and dosimetry parameters, including the scanning speed which is a special feature of synchrotron radiotherapy as the beam is much thinner than a typical target. One can question the instantaneous speed variability measured with the interferometer; however, the average dose measurements are not adversely affected and no suspicious dose variations in the vertical direction were observed on dose profiles obtained with radiochromic films (Livingstone *et al.*, 2016). Additionally, the large instantaneous variations in velocity as measured by the interferometer are due partly to the high sample rate of the unit. For a more realistic comparison, measurements should be performed at a sampling rate more relevant to the dosimetric measurements. For example, for a 0.5 mm beam height and  $1 \text{ mm s}^{-1}$  scanning velocity, the transition time between the aperture edges is 500 ms. Performing a rolling time average of the corresponding data from Table 1 yields a dose variation of <1% compared with the 19.7% instantaneous dose variation reported. It can be concluded that the instantaneous velocity

variations are not important for the dosimetry. However, a future interlock on the stage velocity for patient safety would need to have a very fast response time (of the order of a few milliseconds) in order to minimize the dose received in an adverse event in a high-dose-rate environment. The large variations in instantaneous velocity could be important in this respect and methods to minimize the instantaneous velocity variations may need to be conceived.

The dose-rate for a given field size is reproducible and quasi-independent of beam height, with a <4% variation observed. A higher dose-rate was consistently measured for the 1 mm beam height compared with the 0.5 or 2 mm. Due to vertical roll-off in the beam (Stevenson *et al.*, 2017), the dose rate is expected to decrease slightly with increasing beam height due to averaging

**Figure 12**

Images from the MRI follow-up of the three tumour-bearing rats. The control rat was euthanised before the end of the study. The number of days refers to time after tumour implantation.

over the height of the beam. The lower dose-rate for the 0.5 mm beam height compared with 1 mm is probably due to BDA centring uncertainties. Consequently, it is critical to accurately centre the BDA on the beam, particularly for the smallest beam heights. It is also important to perform dosimetric measurements for the required treatment conditions immediately before treatments. This study reports dose rates in broad and spatially fractionated beams using the commonly used filtration ('F4', 94 keV mean weighted energy, 3 T wiggler field). The maximum dose rate at 20 mm depth in this configuration is  $\sim 240 \text{ Gy s}^{-1}$ ; however, dose rates as high as  $8\text{--}10 \text{ kGy s}^{-1}$  are reported for MRT studies at the ESRF (Bräuer-Krisch *et al.*, 2015). The IMBL dose rate can be increased by increasing the wiggler field to its maximum (4 T) and by changing the filtration, which also means changing the spectrum. In that case, dose rates of several  $\text{kGy s}^{-1}$  could be achieved at IMBL (Stevenson *et al.*, 2017).

The key dose parameters for synchrotron radiotherapy have been successfully characterized for fields down to  $5 \text{ mm} \times 5 \text{ mm}$ . These include the broad-beam peak and valley depth doses, PVDR as a function of depth and field size, and collimator output factors as a function of depth, collimator type and field size.

This paper also reports an *in vivo* oncology feasibility study performed on the preclinical radiotherapy stage available at IMBL. This includes dosimetry, irradiation with two different collimators and imaging follow-up. The dosimetry was first performed under full scatter conditions in a water tank at the target depth for the treatment field size. The dose rates were also checked in a rat-head-sized phantom to study whether the measurements were impaired by a lack of backscatter. The dose rate at 10 mm depth for a  $10 \text{ mm} \times 10 \text{ mm}$  field without spatial fractionation was  $264 \text{ Gy s}^{-1}$  under full scatter conditions and  $259 \text{ Gy s}^{-1}$  in the cylindrical small-animal phantom which shows that the differences are within the measurement uncertainties. It is thus possible to rely on standardized absorbed dose to water measurements acquired with the dedicated preclinical stage.

This is the first *in vivo* end-to-end study reported on such a fully integrated preclinical stage for synchrotron radiotherapy. The type of experiment reported in this paper as a feasibility study is of particular interest to study how the dose can be prescribed in spatially fractionated fields. Indeed, for multiport or crossfired irradiations there is a real need to understand whether the dose should be prescribed as the minimum value delivered *via* the valley doses, an integrated dose or the superposition of peak doses. However, these preclinical studies need a much larger animal cohort to be conclusive. The reproducibility, ease and fast delivery of treatment protocols on the preclinical stage will allow such studies. Other preclinical studies are currently performed using this device to study healthy tissue effects of high-dose-rate irradiations with and without spatial fractionation, on various organs such as mammary gland, brainstem, abdomen and lung. These studies are required for the safe transfer of these innovative radiotherapy techniques to clinical use.

## 5. Conclusion

The main achievement presented in this paper is that the IMBL preclinical synchrotron radiotherapy irradiation stage provides unique opportunities for reproducible radiobiology studies in small animals to answer fundamental questions on biological pathways in high-dose-rate synchrotron radiotherapy. This tool is also a unique opportunity to set the medical physics codes of practice for spatially fractionated submillimetric beams, such as dosimetry protocols, treatment planning benchmarking platform, patient safety procedures and patient safety systems. All the above-mentioned studies are mandatory for a better understanding of biological responses for radiotherapy using spatially fractionated fields and will definitely pave the way to clinical trials.

## Acknowledgements

This research was undertaken on the Imaging and Medical beamline at the Australian Synchrotron, Victoria, Australia. IMBL scientists acknowledge financial support from the National Health and Medical Research Council (NHMRC). JCC acknowledges support by an NHMRC Project Grant (APP1061772). JFA, YP and FP were financially supported by the Institut National de la Santé et de la Recherche Médicale (INSERM) 'Domaine de la physique, des mathématiques ou des sciences de l'ingénieur appliqués au Cancer' PC201327 grant. JL and JFA acknowledge support from the Laboratory of Excellence (LabEx) PRIMES (Physics, Radiobiology, Medical Imaging and Simulation) ANR-11-LABX-0063/ANR-11-IDEX-0007 program. JFA also acknowledges short-term scientific mission funding from the European Cooperation in Science and Technology (COST) Biomedicine and Molecular Biosciences action TD1205. The authors also thank N. Afshar, C. Dingfelder, A. Maksimenko, P. Martin, J. Pearson, T. Smith, M. Stephenson, A. Walsh, Z. Wang and Q. Wu for their contributions to this project.

## References

- Balosso, J., Estève, F., Elleaume, H., Bravin, A., Adam, J.-F., Renier, M., Nemoz, C., Brochard, T., Berkvens, P. & Le Bas, J.-F. (2014). *Radiother. Oncol.* **111**, S81–S82.
- Bartzsch, S. & Oelfke, U. (2013). *Med. Phys.* **40**, 111714.
- Bouchet, A., Lemasson, B., Christen, T., Potez, M., Rome, C., Coquery, N., Le Clec'h, C., Moisan, A., Bräuer-Krisch, E., Leduc, G., Rémy, C., Laissue, J. A., Barbier, E. L., Brun, E. & Serduc, R. (2013). *Radiother. Oncol.* **108**, 143–148.
- Bouchet, A., Potez, M. T., Flaender, M., Schaad, L., Rome, C., Farion, R., Laissue, J. A., Djonov, V., Elleaume, H., Brun, E. & Serduc, R. (2016). *Int. J. Radiat. Oncol. Biol. Phys.* **92**, E94–E95.
- Bräuer-Krisch, E., Adam, J.-F., Alagoz, E., Bartzsch, S., Crosbie, J., DeWagter, C., Dipuglia, A., Donzelli, M., Doran, S., Fournier, P., Kalef-Ezra, J., Kock, A., Lerch, M., McErlean, C., Oelfke, U., Olko, P., Petasecca, M., Povoli, M., Rosenfeld, A., Siegbahn, E. A., Sporea, D. & Stugu, B. (2015). *Phys. Med.* **31**, 568–583.

- Crosbie, J. C., Rogers, P. A. W., Stevenson, A. W., Hall, C. J., Lye, J. E., Nordström, T., Midgley, S. M. & Lewis, R. A. (2013). *Med. Phys.* **40**, 062103.
- Deman, P., Vautrin, M., Edouard, M., Stupar, V., Bobyk, L., Farion, R., Elleaume, H., Rémy, C., Barbier, E. L., Estève, F. & Adam, J.-F. (2012). *Int. J. Radiat. Oncol. Biol. Phys.* **82**, e693–e700.
- Dilmanian, F. A., Zhong, Z., Bacarian, T., Benveniste, H., Romanelli, P., Wang, R., Welwart, J., Yuasa, T., Rosen, E. M. & Ansel, D. J. (2006). *Proc. Natl Acad. Sci. USA*, **103**, 9709–9714.
- Donzelli, M., Bräuer-Krisch, E., Nemoz, C., Brochard, T. & Oelfke, U. (2016). *Med. Phys.* **43**, 3157–3167.
- Favaudon, V., Caplier, L., Monceau, V., Pouzoulet, F., Sayarath, M., Fouillade, C., Poupon, M.-F., Brito, I., Hupé, P., Bourhis, J., Hall, J., Fontaine, J.-J. & Vozenin, M.-C. (2014). *Sci. Transl. Med.* **6**, 245ra93.
- Fournier, P., Crosbie, J. C., Cornelius, I., Berkvens, P., Donzelli, M., Clavel, A. H., Rosenfeld, A. B., Petasecca, M., Lerch, M. L. F. & Bräuer-Krisch, E. (2016). *Phys. Med. Biol.* **61**, N349–N361.
- Grotzer, M. A., Schülke, E., Bräuer-Krisch, E. & Laissue, J. A. (2015). *Phys. Med.* **31**, 564–567.
- Ibrahim, M. J., Yang, Y., Crosbie, J. C., Stevenson, A. W., Cann, L., Paiva, P. & Rogers, P. A. (2016). *Radiat. Res.* **185**, 60–68.
- International Atomic Energy Agency (2000). *Absorbed Dose Determination in External Beam Radiotherapy: An International Code of Practice for Dosimetry Based Standards of Absorbed Dose to Water*, Technical Report Series No. 398. Vienna: International Atomic Energy Agency.
- Livingstone, J., Stevenson, A. W., Butler, D. J., Häusermann, D. & Adam, J. F. (2016). *Med. Phys.* **43**, 4283–4293.
- Lye, J. E., Harty, P. D., Butler, D. J., Crosbie, J. C., Livingstone, J., Poole, C. M., Ramanathan, G., Wright, T. & Stevenson, A. W. (2016). *Phys. Med. Biol.* **61**, 4201–4222.
- Martínez-Rovira, I., Sempau, J. & Prezado, Y. (2012). *Med. Phys.* **39**, 2829–2838.
- Pelliccia, D., Crosbie, J. C. & Larkin, K. G. (2016b). *Phys. Med. Biol.* **61**, 5942–5955.
- Pelliccia, D., Poole, C. M., Livingstone, J., Stevenson, A. W., Smyth, L. M. L., Rogers, P. A. W., Häusermann, D. & Crosbie, J. C. (2016a). *J. Synchrotron Rad.* **23**, 566–573.
- Pouyatos, B., Nemoz, C., Chabrol, T., Potez, M., Bräuer, E., Renaud, L., Pernet-Gallay, K., Estève, F., David, O., Kahane, P., Laissue, J. A., Depaulis, A. & Serduc, R. (2016). *Sci. Rep.* **6**, 27250.
- Prezado, Y., Sarun, S., Gil, S., Deman, P., Bouchet, A. & Le Duc, G. (2012). *J. Synchrotron Rad.* **19**, 60–65.
- Prezado, Y., Vautrin, M., Martínez-Rovira, I., Bravin, A., Estève, F., Elleaume, H., Berkvens, P. & Adam, J. F. (2011). *Med. Phys.* **38**, 1709–1717.
- Serduc, R., Bräuer-Krisch, E., Siegbahn, E. A., Bouchet, A., Pouyatos, B., Carron, R., Pannetier, N., Renaud, L., Berruyer, G., Nemoz, C., Brochard, T., Rémy, C., Barbier, E. L., Bravin, A., Le Duc, G., Depaulis, A., Estève, F. & Laissue, J. A. (2010). *PLoS ONE*, **5**, e9028.
- Smyth, L. M. L., Senthil, S., Crosbie, J. C. & Rogers, P. A. W. (2016). *Int. J. Radiat. Biol.* **92**, 302–311.
- Stevenson, A. W., Crosbie, J. C., Hall, C. J., Häusermann, D., Livingstone, J. & Lye, J. E. (2017). *J. Synchrotron Rad.* **24**, 110–141.